



Effect of A- and B-site doping on the low-temperature dielectric and impedance properties of BaTiO₃-based ceramics

Ruifeng Niu¹ · Depeng Wang¹ · Liqi Cui¹ · Weitian Wang¹

Received: 24 April 2023 / Revised: 1 June 2023 / Accepted: 22 June 2023 / Published online: 24 July 2023
© The Korean Physical Society 2023

Abstract

In this work, two series of BaTiO₃-based ceramics, Ba_{1-x}Sr_xTiO₃ ($x=0, 0.2, 0.4, 0.6, 0.8$) and BaTi_{1-x}Ta_xO₃ ($x=0.03, 0.06, 0.075, 0.09, 0.1$), were synthesized by using standard solid-state reaction method. Frequency-dependent dielectric and impedance properties were investigated in low temperature range of 300–100 K. The changes in dielectric properties of Ba_{1-x}Sr_xTiO₃ are believed to originate from the phase transition due to the different A-site Sr²⁺ doping concentration. The local electron-pinned defect-dipole effect is responsible for the enhancement of dielectric constant observed in B-site Ta⁵⁺ doped BaTi_{1-x}Ta_xO₃ ceramics. The complex impedance analysis was used to discern the temperature and frequency dependence of grains and grain boundaries responses. The results suggest the application of A- and B-site doped BaTiO₃ ceramics in the field of dielectric devices at low temperatures.

Keywords Ceramics · Dielectric properties · Impedance analysis

1 Introduction

Traditional ABO₃ perovskite-type oxide materials have attracted extensive interest due to their ferroelectric, piezoelectric, pyroelectric and dielectric properties and potential applications such as storage devices, phase shifters, microelectromechanical systems, multilayer ceramic capacitors and optoelectronic devices [1–4]. Specifically, the notable barium titanate (BaTiO₃, BTO), strontium titanate (SrTiO₃, STO) and their equivalent substitute materials are potential candidates for these applications. It is well known that ion-doping is an effective way to improve the physical properties of oxide materials. For example, the leakage current density, ferroelectric polarization and dielectric loss of BiFeO₃ ceramics have been improved by Dy³⁺ doping [5]. (Bi_{0.5}Na_{0.5})_{0.94}Ba_{0.06}TiO₃ ceramics doped with 0.3 wt% Sm₂O₃ exhibit excellent piezoelectric properties [6]. At room temperature, BTO crystallizes in a tetragonal structure, while STO in a cubic structure. By A-site substitution, Ba_{1-x}Sr_xTiO₃ (BST) ceramics exhibit attractive dielectric properties,

high breakdown strength, and good thermal stability due to the microstructure changes according to the different doping concentration x [7, 8]. It is worth noting that BST is expected to replace silicon dioxide nowadays, which is a traditional dielectric material and can provide the required charge storage density [9]. Moreover, excellent electrical and dielectric properties have been reported for BTO ceramics by B-site substitution with Zr⁴⁺ ions [10]. The radius of Ta⁵⁺ is 0.64 Å, which is smaller than the radius of Zr⁴⁺ (0.72 Å), and closer to the radius of Ti⁴⁺ (0.61 Å). This makes the studies on the dielectric and impedance properties of BaTi_{1-x}Ta_xO₃ (BTT) are well worth looking into. In low-temperature applications, BST and BTT materials have shown great potential in a variety of fields, including superconducting electronics and low-temperature electronics [11–13]. For instance, BST and BTT materials can be used to manufacture superconducting inductors, which are commonly employed in low-temperature magnet systems and superconducting quantum interference devices [14]. In addition, their high dielectric constants at low temperatures make them ideal for producing low-temperature capacitors, which are widely used in

✉ Weitian Wang
wtwang@ytu.edu.cn

¹ School of Physics and Electronic Information, Yantai University, 264005 Yantai, People's Republic of China

low-temperature electronic experiments and applications [15].

Considering the size of doping ions, the A- and B-site substitution in ABO_3 perovskite-type oxides is controlled by an allowable tolerance factor [16, 17],

$$\tau = \frac{r_A + r_O}{\sqrt{2}(r_B + r_O)},$$

where r_A and r_B represent the radii of the ions at position A and B, respectively, r_O is the radius of the ion at position O. If the factor τ is within the range of 0.77–1.10, the atoms on A or B sites can be replaced by the doping ions to form a continuous solid solution. The calculated values of τ for BST and BTT are 1.06–1.00 and 1.06–1.04, respectively, suggesting these materials are available substitution-doping oxides. In this paper, perovskite-type BST and BTT ceramics with various doping concentrations were fabricated by using solid-state reaction method. The effect of A- and B-site doping on the dielectric and impedance properties of BTO-based ceramics was investigated at low temperatures.

2 Experimental details

2.1 BST ceramics synthesis

$Ba_{1-x}Sr_xTiO_3$ ceramics were synthesized by solid-state reaction using high-pure $BaCO_3$, $SrCO_3$ and TiO_2 as raw materials. Five samples were prepared by setting $x = 0, 0.2, 0.4, 0.6, 0.8$, and the corresponding labels were denoted as BST00, BST02, BST04, BST06, and BST08, respectively. The stoichiometric powders were weighed by using electronic precision balance and were fully mixed and milled to produce a uniform mixture, which was placed in an alumina crucible and pre-sintered in a Muffle furnace at 1350 °C for 4 h to synthesize BST powders. The ground powders were placed in a cylindrical matrix and pressed uniaxial at a pressure of 10 MPa to obtain high-density pellets with a diameter of 10 mm and a thickness of 3 mm, which were sintered at 1400 °C for 10 h to fabricate BST ceramics samples.

2.2 BTT ceramics synthesis

The ceramic $BaTi_{1-x}Ta_xO_3$ samples were prepared through conventional solid-state reaction process, using TiO_2 (99.9%), $BaCO_3$ (99.99%) and Ta_2O_5 (99.8%) raw materials. Five samples were prepared by setting $x = 0.03, 0.06, 0.075, 0.09, 0.1$, and the corresponding labels

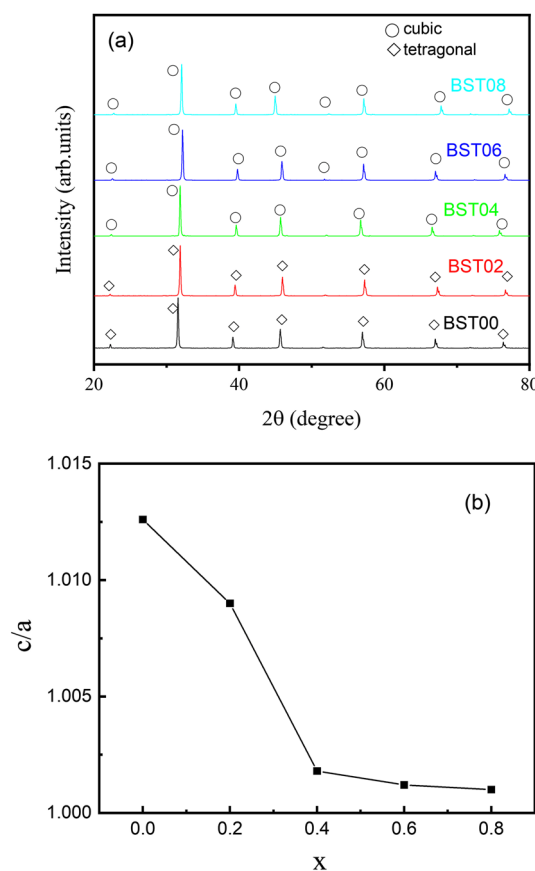


Fig. 1 **a** XRD patterns of the synthesized BST ceramics. **b** The variation of c/a with the concentration x

were denoted as BTT03, BTT06, BTT075, BTT09, and BTT10, respectively. The stoichiometric raw materials were ground and mixed in an agate mortar, then calcined at a temperature of 1300 °C for 4 h. By dry pressing under a pressure of 8 MPa, a disk with a diameter of 10 mm and a thickness of about 3 mm is formed. After sintering at 1400 °C for 10 h, BTT ceramic samples with bulk density greater than 95% were obtained.

2.3 Characterization and measurements

The crystallization of the fabricated BST and BTT samples was analyzed by X-ray diffraction (XRD) using a Rigaku diffractometer with $Cu K\alpha$ radiation source with a Ni filter. For dielectric and impedance measurements, silver electrodes with a 0.2-mm diameter were sputtered on both sides of the samples by using a shadow mask. Low-temperature dependence of complex dielectric properties was measured on a QuadTech 1730 LCR Digibridge over a frequency range of 100 Hz–1 MHz. The impedance

spectroscopy was examined by using a HP4194A analyzer with signal amplitude of 50 mV. Data were taken in a temperature range of 300–100 K.

3 Results and discussion

3.1 XRD analysis

Figure 1a shows the XRD patterns of the fabricated BST ceramic samples with different x values. The peaks of BST00 and BST02 can be indexed to a tetragonal perovskite phase with space group $P4mm$, while the peaks of BST04, BST06, and BST08 are related to a cubic phase with space group $Pm\bar{3}m$. This structural change means the prepared BST samples transform from the ferroelectric state to paraelectric state when $x \geq 0.4$. The calculated values of lattice constants a and c are listed in Table 1. The variation of c/a with the Sr^{2+} concentration x is plotted in Fig. 1b, which clearly demonstrates the phase transformation.

The XRD patterns of the BTT samples are shown in Fig. 2a. All the diffraction peaks can be indexed to a tetragonal phase, and no impurity could be detected indicating that B-site doping of Ta^{5+} with 10 at% concentration does not change the structure of BTO seriously. However, it is observed that the diffraction peaks shift to lower degree with the increase of Ta^{5+} doping. This trend is manifested by the locations of (101) peaks shown in Fig. 2b. The increased interplanar spacings are believed to be the causes for the variation of diffraction peak positions. The calculated values of lattice constants a and c are listed in Table 2. Figure 2c shows the schematic illustration of B-site doping BTT crystal structure. As is known, the size of Ta^{5+} is larger than that of Ti^{4+} . Doping with larger ions will lead to the increased lattice constant, which is responsible for the shift of diffraction peaks.

3.2 Dielectric measurements

Figure 3 shows the dielectric properties of BST ceramic samples measured at room temperature in the frequency range of 100 Hz–1 MHz. For all the samples, the values of dielectric constant and loss decrease with the increase of frequency, and reach a constant state when the testing frequency is over 10 kHz. This is caused by the weak electron

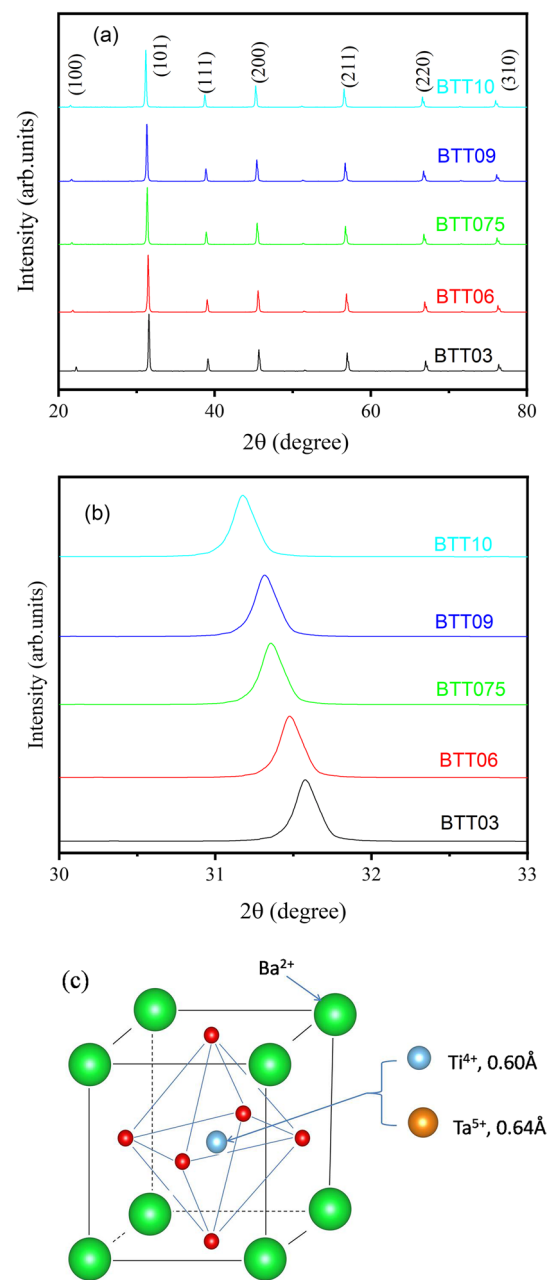


Fig. 2 a XRD patterns of the synthesized BTT ceramics. b Shift of (101) peaks. c Sketch of BTT crystal structure

polarization at high frequencies [18, 19]. By Sr^{2+} doping, BST02 exhibits large dielectric constant, as shown in Fig. 3a. With a further increase of doping, the values of dielectric

Table 1 The calculated a and c values of the BST ceramic samples

	BST00	BST02	BST04	BST06	BST08
a (Å)	3.994	3.990	3.912	3.910	3.908
c (Å)	4.038	4.025	3.919	3.914	3.911

Table 2 The calculated a and c values of the BTT ceramic samples

	BTT03	BTT06	BTT075	BTT09	BTT10
a (Å)	3.996	3.998	4.008	4.010	4.022
c (Å)	4.040	4.042	4.052	4.054	4.066

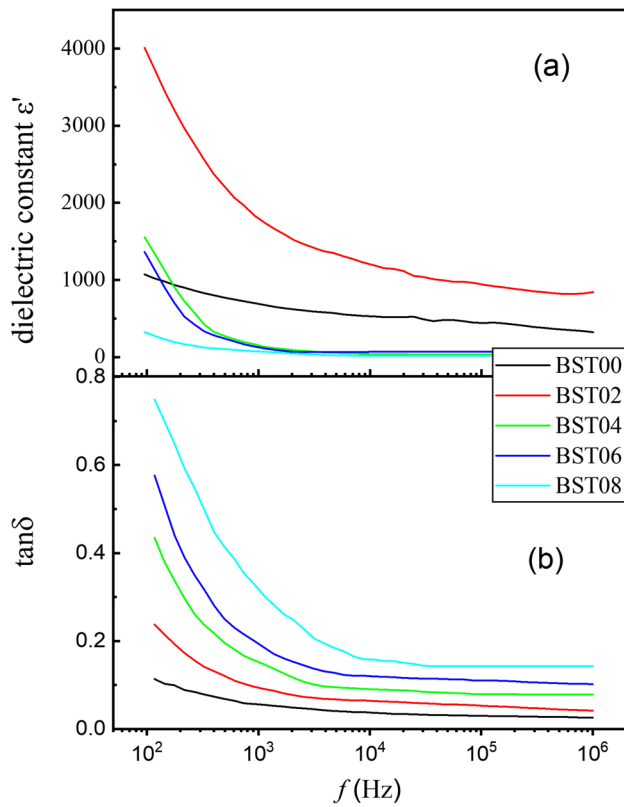


Fig. 3 Frequency-dependent dielectric constant and loss for the BST samples at room temperature

constant for BST04, BST06, and BST08 decrease as a result of phase transformation. As shown in Fig. 3b, the dielectric loss of the BST samples is between 0.00257–0.748, and the dielectric loss increases with the increase of Sr ion doping. The defects and oxygen vacancies produced during the doping process play a role for this result [20].

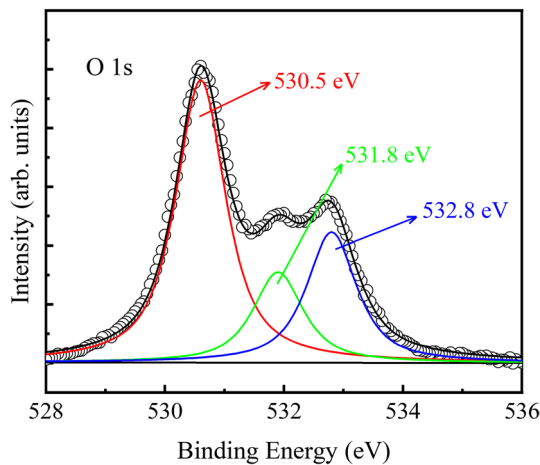


Fig. 4 Core level XPS spectra of O 1s for BST06

In order to check the defects in BST samples, X-ray photoelectron spectroscopy (XPS) of elemental O in BST06 is provided in Fig. 4. The O 1s spectrum can be resolved into three peaks at 530.5, 531.8, and 532.8 eV, which can be attributed to lattice oxygen, oxygen defects, and surface-adsorbed oxygen species, respectively [21, 22]. The existing oxygen defects are believed to be responsible for the increased dielectric loss of BST ceramics with increasing Sr^{2+} ion content. Moreover, theoretical calculations predict a number defect states within the BST band gap [23]. The formation of these defects is attributed to vacancies on the Ba and Sr as well as the O site of the BST lattice. The band gap of BST increases with the increased doping of Sr^{2+} ion. More defect states can lead to the increased dielectric loss.

Generally, the exponential growth of dielectric loss indicates that relaxation is related to the jump of carrier ions and the appropriate relaxation of surrounding ions. This behavior can be described by a Universal Dielectric Response (UDR) model [24],

$$f\epsilon' = f\epsilon_{\infty} + \frac{A}{\epsilon_0} \tan\left(\frac{s\pi}{2}\right) f^s, \quad (1)$$

and

$$f\epsilon'' = \frac{A}{\epsilon_0} f^s, \quad (2)$$

where ϵ_{∞} is the high-frequency value of $\epsilon'(\omega)$, ϵ_0 is the electric permittivity of free space, A and s are constants.

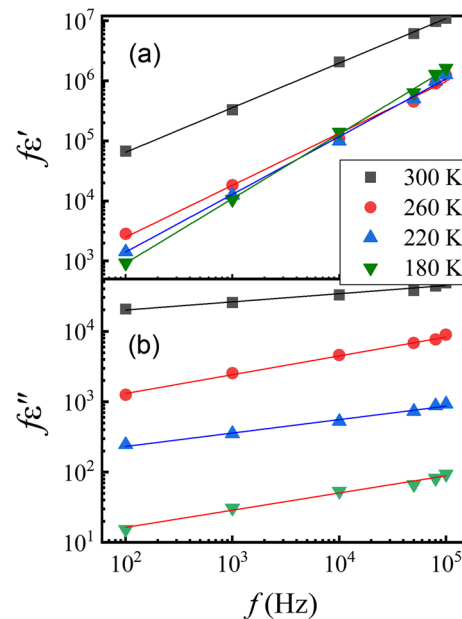


Fig. 5 Logarithmic diagram of frequency dependence of $f\epsilon'$ and $f\epsilon''$ for BST04 sample at given temperatures

According to Eqs. (1) and (2), a straight line with a slope of s should be obtained in the plot of $\log f \epsilon'$ versus $\log f$ and $\log f \epsilon''$ versus $\log f$ at a given temperature. This relationship was confirmed by the log–log graph for BST04 sample shown in Fig. 5. By linear fitting, the plot of $\log f \epsilon'$ versus $\log f$ (Fig. 5a) gives $s \sim 0.74$, while that of $\log f \epsilon''$ versus $\log f$ (Fig. 5b) gives $s = 0.26\text{--}0.28$. The obtained values of s are consistent with the UDR assumption [25]. The s value is an important dielectric property parameter that reflects the polarizability, complexity, and frequency response characteristics of the dielectric material. For BST and BTT perovskite oxide materials, the s value usually reflects the complexity of the internal structure and the influence of non-linear polarization behavior. Specifically, the s value can be used to evaluate the polarization capability, frequency response characteristics, and nonlinear polarization behavior of the dielectric material. The obtained s value gives a better understanding of the dielectric properties of these materials, and a theoretical basis can be provided for their applications.

Figure 6 shows the temperature-dependent dielectric constant of the prepared samples at $f = 10$ kHz in the low temperature range of 300–100 K. The peaks for BST04, BST06, and BST08 suggest the Curie temperature $T_c = 265$, 190, 150 K, respectively. When the temperature is lower than T_c , the BST ceramics will spontaneously polarize, and the dipole will act to form the internal battery. However, when the temperature is higher than T_c , the BST ceramics act in a paraelectric phase and the dipole direction of the element is irregular, and the dielectric polarization and dielectric constant decrease with the increase of temperature [26]. As is known, with the decrease doping concentration of Sr^{2+} , T_c of BST shifts to higher temperature. For BST02 and BST00, the Curie transition temperature is not in the low temperature

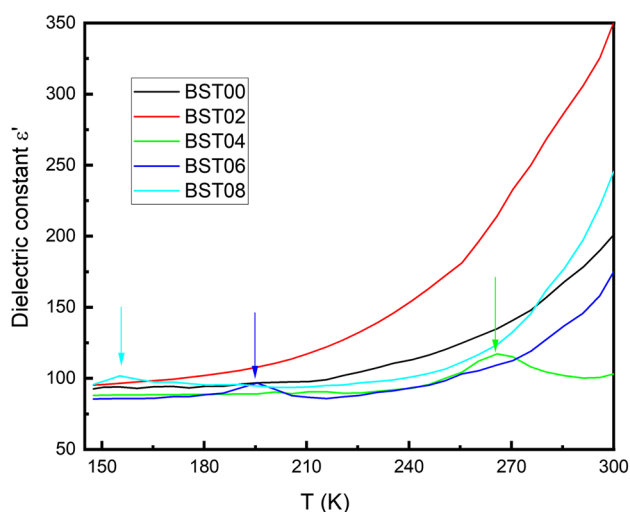
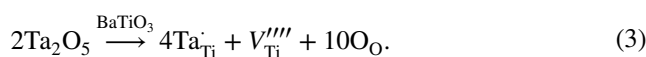


Fig. 6 Temperature-dependent dielectric constant of BST samples at $f = 10$ kHz

range of our experiment. It has been reported that the variation of T_c of ABO_3 ceramics is related to the average ionic radius of the A-site cation [27]. The substitution of Ba^{2+} ion (1.35 Å) with Sr^{2+} ion (1.18 Å) will reduce the average ionic radius, thus stabilize the cubic phase, which leads to the decrease of T_c with the increase doping of Sr^{2+} .

Figure 7 shows the dielectric constant and loss as a function of frequency for BTT samples at room temperature. It can be seen that the dielectric properties are weakly dependent of the testing frequency except for BTT10. The dielectric constant of BTT10 increases significantly with the decrease of frequency, and a loss peak appears around $f = 7$ kHz (Inset of Fig. 7).

The increase of dielectric constant of BTT10 is attributed to the generation of electron traps, which can be expressed as,



When the doping concentration of Ta^{5+} increases, it is expected that Ta^{5+} ions will gather at the grain boundary because of the driving force of electrostatic force and elastic strain energy. Therefore, the positively charged grain-boundary cores will be produced due to the charged defects Ta_{Ti} . The charged defects, giving rise to large defect-dipole clusters, are responsible for the large dielectric constant of BTT10 at lower frequencies. The loss peak of BTT10 in the inset of Fig. 7 is believed to be related to the relaxation process of defect-dipoles and double ionization of oxygen vacancies. When the Ta^{5+} doping concentration is lower than 10%, the electron-pinned defect-dipoles are not rich enough for the increase of the dielectric constant, and the dielectric behaviors of BTT03, BTT06, BTT075, and BTT09 show approximate independence of the testing frequency.

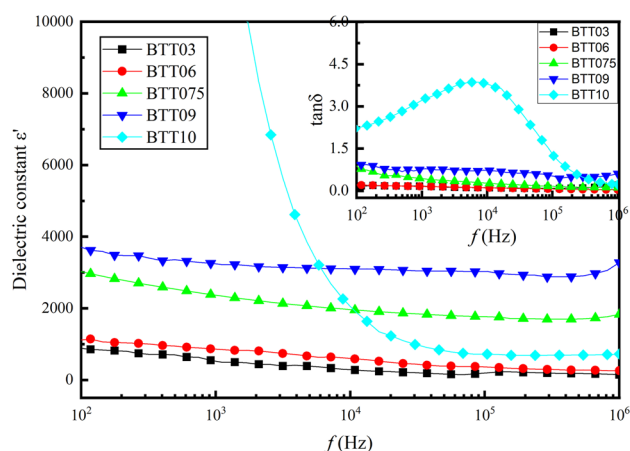


Fig. 7 Frequency-dependent dielectric constant and loss (inset) for the BTT samples at room temperature

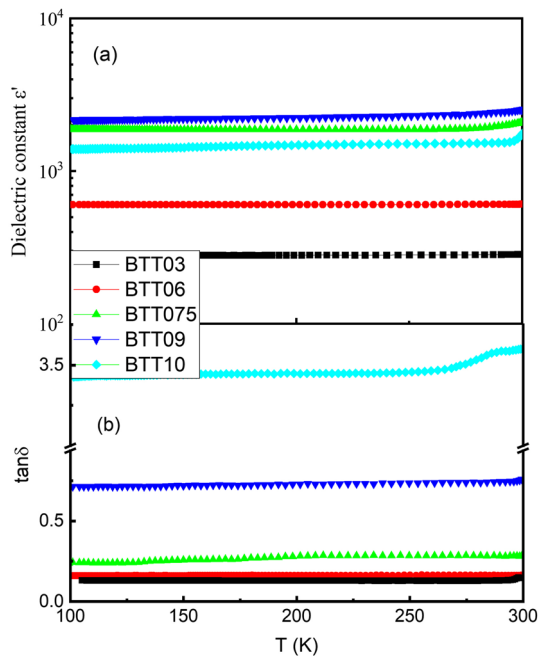


Fig. 8 Temperature-dependent **a** dielectric constant and **b** loss of BTT samples at $f=10$ kHz

Moreover, at lower doping level of Ta^{5+} , the dielectric properties of BTT samples exhibit good low-temperature stability. Figure 8 shows the temperature dependence of dielectric constant and loss of BTT samples at $f=10$ kHz. The values of dielectric constant and loss are almost independent of the temperatures in the range of 100–300 K. The changing rate of dielectric constant, defined by $r_{\epsilon} = \frac{\epsilon(T) - \epsilon(300 \text{ K})}{\epsilon(300 \text{ K})} \times 100\%$, is below 19%, and that of dielectric loss, defined by $r_{\tan \delta} = \frac{\tan \delta(T) - \tan \delta(300 \text{ K})}{\tan \delta(300 \text{ K})} \times 100\%$, is below 5.5% for all the samples. The good temperature stability suggests the low temperature coefficient of dielectric properties, which may expand the application of Ta-doped BTO materials to low-temperature fields.

3.3 Impedance analysis

Impedance analysis is considered to be an effective tool to study the dielectric behavior of ceramics materials at the microscopic level [28]. By plotting the relationship between Z' and Z'' , several arcs will appear at different frequencies depending on the relaxation time, where Z' and Z'' are real and imaginary parts of complex impedance Z^* . As the relaxation time of grains is shorter than that of grain boundaries, the arc corresponding to the grain effect locates at the higher frequency, while that corresponding to the grain boundary effect locates at the lower frequency. Figure 9 shows typical Z' versus Z'' plots for BST04 sample at different

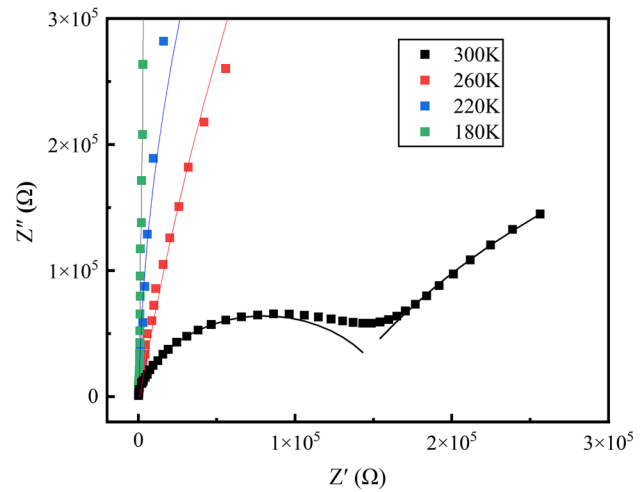


Fig. 9 Typical Z' versus Z'' plots for BST04 sample at different temperatures

temperatures in a frequency range of 100 Hz–1 MHz. At 300 K, two arcs corresponding to grain and grain boundary effects appear. The radii of these arcs increase dramatically with the decrease of the temperature, indicating the increase of grain and grain boundary resistance at low temperatures. The arcs at 260, 220, 180 K are not completely presented in the impedance spectrum, which means the impedance responses of grain and grain boundary fall out of the scope of measuring frequencies.

The complex impedance spectra of BTT samples at room temperature are shown in Fig. 10. The plot for BTT10 displays two arcs, corresponding to the responses of grains and grain boundaries. With the decrease of Ta^{5+} doping concentration, the resistance of grains and grain boundaries increases, resulting in the enlarged arcs on the impedance plane. As is known, the stoichiometric BTO is an insulator

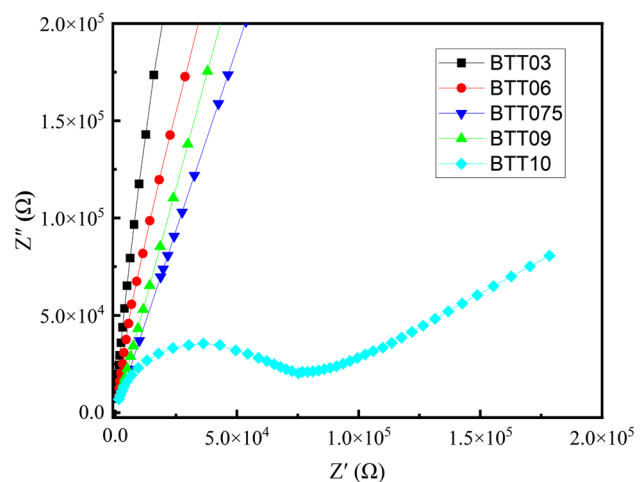


Fig. 10 Z' versus Z'' plots for the BTT samples at room temperature

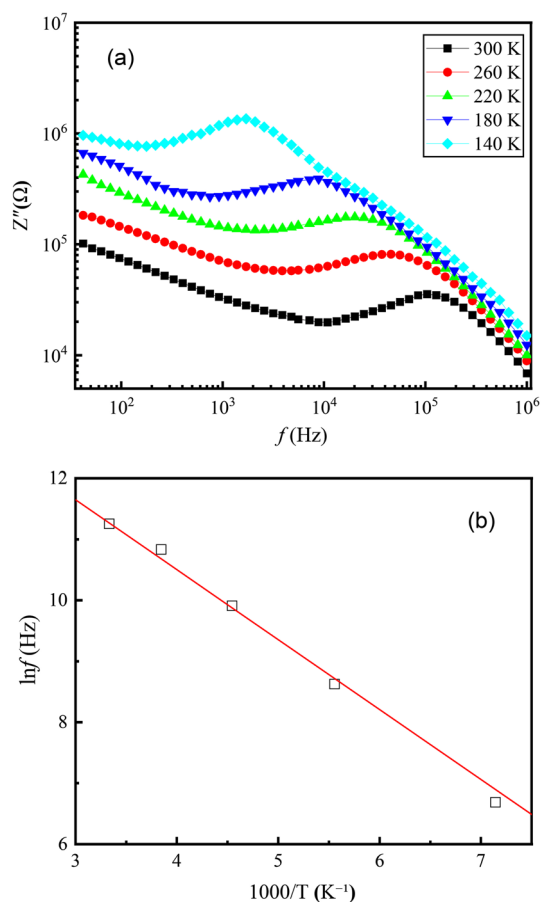


Fig. 11 **a** Frequency-dependent Z'' of BTT10 at different temperatures. **b** Arrhenius plots for the BTT10 sample

with large resistance. However, defects and electron donors will be inevitably produced during the substitution of Ti^{4+} with Ta^{5+} ions. The existing carriers at high doping concentrations will result in the reduction of grains and grain boundaries resistance, which is responsible for the observed two arcs for BTT10.

To further analyze the impedance properties of BTT10, the frequency-dependent Z'' at different temperatures is shown in Fig. 11a. It can be seen that the value of Z'' decreases with the increase of temperature. This phenomenon can be explained by the fact that the energy of the polaron in ceramic materials increases with the increase of temperature, which makes it easier to carry out long-range or short-range hopping, leading to the reduction of Z'' .

Moreover, the relaxation peaks, which move to higher frequency with the increase of temperature, appear in the curves indicating the relaxation process is a thermal activation mechanism. Generally, the relationship between relaxation frequency f and corresponding temperature T conform to Arrhenius formula [29, 30]

$$f = f_0 \exp\left(-\frac{E_a}{K_B T}\right), \quad (4)$$

where f_0 is the preexponential factor, K_B is the Boltzmann constant, and E_a is activation energy. Relaxation peak position versus $1/T$ is shown in Fig. 11b. By linear fitting, the activation energy of BTT10 is 1.14 eV. The relaxation activation energy is mainly the free energy of carriers jumping between adjacent lattices. According to previous studies, the relaxation energy caused by oxygen vacancy double ionization is between 0.6 and 1.2 eV, while the relaxation energy caused by oxygen vacancy single ionization is less than 0.6 eV in perovskite ceramics [31–33]. When the relaxation activation energy is greater than 1.2 eV, it is mainly due to cation defects. It can be seen that the relaxation process of BTT10 ceramic sample is related to the double ionization of oxygen vacancy.

4 Conclusion

Perovskite-type oxide materials $Ba_{1-x}Sr_xTiO_3$ ($x=0, 0.2, 0.4, 0.6, 0.8$) and $BaTi_{1-x}Ta_xO_3$ ($x=0.03, 0.06, 0.075, 0.09, 0.1$) were synthesized by using standard solid-state reaction method. Effect of A- and B-site doping on the low-temperature dielectric and impedance properties of $BaTiO_3$ -based ceramics was studied. The Curie temperature of $Ba_{1-x}Sr_xTiO_3$ ceramics shifts to lower temperature with the increase of Sr^{2+} doping concentration. The phase transition and the existing oxygen vacancies are responsible for the observed dielectric properties. For $BaTi_{1-x}Ta_xO_3$ ceramics, B-site Ta^{5+} doping up to 10 at% concentration does not change the crystal structure seriously. As the electronegativity of Ti^{4+} and Ta^{5+} is different, the local electron-pinned defect-dipole effect plays a role for the different appearance of dielectric constant and relaxation peak for the BTT10 sample. In addition, we investigated the low-temperature impedance properties of the prepared samples. The grain and grain boundary resistance of $Ba_{1-x}Sr_xTiO_3$ ceramics increases with the decrease of the temperature, while that of $BaTi_{1-x}Ta_xO_3$ ceramics decreases with the increase doping of Ta^{5+} ion. The produced carriers at high doping concentration of pentavalent ion can be used to explain the results. The significant impact of A-site and B-site doping on the low-temperature dielectric and impedance properties of $BaTiO_3$ -based ceramics demonstrated in our study provides important insights into the physical properties of these materials and has implications for the development of new electronic devices.

References

1. A. Ioachim, R. Ramer, M.I. Toacsan, M.G. Banciu, L. Nedelcu, C.A. Dutu, F. Vasiliu, H.V. Alexandru, C. Berbecaru, G. Stoica, *J. Eur. Ceram. Soc.* **27**, 1177 (2007)
2. C.L. Huang, J.J. Wang, B.J. Li, W.C. Lee, *J. Alloy. Compd.* **461**, 440 (2008)
3. T. Lim, O.S. Jeon, Y. La, S.Y. Park, Y.J. Yoo, K.H. Yang, *J. Korean Phys. Soc.* **77**, 1021 (2020)
4. J.S. Kim, H.S. Lee, *J. Korean Phys. Soc.* **75**, 476 (2019)
5. P. Murugavel, J.H. Lee, D. Lee, S.Y. Jang, T.W. Noh, Y. Jo, *Appl. Phys. Lett.* **90**, 14292 (2007)
6. F. Peng, Z. Xu, R. Chu, L. Wei, G. Zang, J. Hao, *Mater. Chem. Phys.* **124**, 1065 (2010)
7. R.L. Hong, K.H. Yoon, E.S. Kim, *Jpn. J. Appl. Phys.* **42**, 6168 (2003)
8. C.H. Lee, Y.J. Oh, D.Y. Lee, D.J. Choi, *J. Korean Phys. Soc.* **69**, 1571 (2016)
9. H.W. You, J.H. Koh, *Jpn. J. Appl. Phys.* **45**, 6362 (2006)
10. S.Y. Chung, D.Y. Yoon, S. Kang, *Acta Mater.* **50**, 3361 (2002)
11. X. Liu, H. Li, M. Qin, *J. Mater. Sci. Mater. Electron.* **28**, 3291 (2017)
12. Q. Zhang, X. Chen, J. Liu, *J. Alloy. Compd.* **665**, 189 (2016)
13. X. Wang, H. Xu, J. Li, *J. Mater. Sci. Mater. Electron.* **31**, 7329 (2020)
14. T. Yamamoto, T. Nakamura, *Supercond. Sci. Technol.* **31**, 043001 (2018)
15. W. Wei, W. Li, L. Li, *J. Mater. Sci. Mater. Electron.* **30**, 4964 (2019)
16. A.J. Feighery, J.C. Abrantes, J.A. Labrincha, J.M. Ferreira, J.R. Frade, *Sensor. Actuat. B Chem.* **75**, 88 (2001)
17. X. Guo, Y. Pu, W. Wang, J. Ji, M. Yang, R. Shi, J. Li, *J. Alloy. Compd.* **818**, 152866 (2020)
18. X. Zhu, J. Zhu, S. Zhou, Z. Liu, N. Ming, *J. Cryst. Growth* **310**, 434 (2008)
19. S. Kongtaweelert, D.C. Sinclair, S. Panichphant, *Curr. Appl. Phys.* **6**, 474 (2006)
20. K.M. Hung, W.D. Yang, C.C. Huang, *J. Eur. Ceram. Soc.* **23**, 1901 (2003)
21. X.B. Chen, L. Liu, P.Y. Yu, S.S. Mao, *Science* **331**, 746 (2011)
22. G. Ou, Y. Xu, B. Wen, R. Lin, B. Ge, Y. Tang, Y. Liang, C. Yang, K. Huang, D. Zu, R. Yu, W. Chen, J. Li, H. Wu, L. Liu, Y. Li, *Nat. Commun.* **9**, 1302 (2018)
23. J. Daniels, R. Wernicke, *Phillips Res. Rep.* **31**, 544 (1976)
24. A.K. Jonscher, *Nature* **267**, 673 (1977)
25. N. Bonanos, R.K. Slotwinski, *J. Mater. Sci.* **19**, 785 (1984)
26. G. Brankovi, Z. Brankovi, M. Cilense, J.A. Varela, *Mater. Sci. Eng B* **122**, 140 (2005)
27. A. Kumari, B. Dasgupta Ghosh, *Adv. Polym. Tech.* **37**, 2270 (2018)
28. D.C. Sinclair, A.R. West, *J. Mater. Sci.* **29**, 6061 (1994)
29. X. Guo, Y. Pu, W. Wang, L. Zhang, J. Ji, R. Shi, Y. Shi, M. Yang, J. Li, *ACS Sustain. Chem. Eng.* **7**, 13041 (2019)
30. L. Zhang, Y. Pu, M. Chen, T. Wei, W. Keipper, R. Shi, X. Guo, R. Li, X. Peng, *J. Eur. Ceram. Soc.* **40**, 71 (2020)
31. L. Liu, Y. Huang, C. Su, L. Fang, M. Wu, C. Hu, H. Fan, *Appl. Phys. A Mater.* **104**, 1047 (2011)
32. C. Veridier, F.D. Morrison, D.C. Lupascu, J.F. Scott, *J. Appl. Phys.* **97**, 1387 (2005)
33. Z. Abdelkafi, N. Abdelmoula, H. Khemakhem, O. Bidault, M. Maglione, *J. Appl. Phys.* **100**, 323 (2006)

Publisher's Note Springer Nature remains neutral with regard to jurisdictional claims in published maps and institutional affiliations.

Springer Nature or its licensor (e.g. a society or other partner) holds exclusive rights to this article under a publishing agreement with the author(s) or other rightsholder(s); author self-archiving of the accepted manuscript version of this article is solely governed by the terms of such publishing agreement and applicable law.